Research Article | Vol. 33, No. 18 / 8 Sep 2025 / Optics Express 38898
Optics EXPRESS

System calibration for single-wavelength multi-terabit mode-division multiplexing free-space optical communication systems

YIMING LI,[1,2,*] GIL FERNANDES,[3] DAVID BENTON,[1] ANTONIN BILLAUD,[4] MARCO FERNANDES,[3] MOHAMMED PATEL,[1] FERNANDO GUIOMAR,[3] AND ANDREW ELLIS[1]

[1]Aston Institute of Photonic Technologies, Aston University, Birmingham B4 7ET, UK
[2]Shanghai Institute of Optics and Fine Mechanics, Chinese Academy of Sciences, Shanghai 201800, China
[3]Instituto de Telecomunicações, University of Aveiro, Aveiro 3810-193, Portugal
[4]Cailabs, 1 Rue Nicolas Joseph Cugnot, Rennes 35000, France
[*]liyiming@siom.ac.cn

Abstract: In this paper, we propose a optical calibration strategy to support a single-wavelength mode-division multiplexing multiple-input multiple-output free-space optical communication system utilising 6 Hermite-Gaussian modes. To minimise the inter-mode crosstalk, higher-order modes at the receiver were exploited to calibrate the optical setup. The signal distortions were minimised for 80 GBaud signals by employing Volterra pre-distortion. Probabilistically-shaped 256-QAM signals were transmitted to maximise the achievable information rate. As a result, this system obtained a record-high achievable information rate of 4.49 Tbit/s/λ in free-space optical communications.

1. Introduction

Mode-division multiplexing (MDM) is a promising technology to extend the capacity limits in free-space optical (FSO) communication systems [1]. Orthogonal to other degrees of freedom such as amplitude [2], phase [3], polarisation [4] and wavelength [5], MDM offers the spatial degree of freedom for multiplexing, extending capacity beyond the conventional limit in both FSO and fibre communications [1,6]. Further to the conventional employment of orbital angular momentum (OAM) modes [1], which constitute an incomplete basis, there is growing interest in employing complete mode basis, such as Hermite-Gaussian (HG) or Laguerre-Gaussian (LG) modes [7,8], to maximise potential capacity gains in the spatial domain [9].

In contrast to fibre communications, FSO communication systems require stringent alignment to maximise received power [10]. In MDM systems, there is an additional requirement of minimising inter-mode crosstalk [11], thus increasing the demand for precise alignments. Otherwise, the MDM systems would be constrained by practical inter-mode crosstalk and inter-symbol interference (ISI), and a considerable performance degradation would be observed when compared with the single-input single-output (SISO) counterparts, resulting in limited symbol rate and constellation complexity [1,12,13]. Consequently, pure MDM FSO systems have demonstrated only marginal improvements in aggregate line rates when compared with SISO FSO systems [1,12]. These results highlight the necessity for precise optical and digital signal processing (DSP) algorithm calibration to further improve the performance of MDM FSO communication systems.

In this paper, we propose a novel optical calibration strategy for a 6×6 MDM FSO communication system using the 6 lowest order HG modes. By employing multi-plane light conversion

#569397 https://doi.org/10.1364/OE.569397
Journal © 2025 Received 2 Jun 2025; revised 11 Aug 2025; accepted 16 Aug 2025; published 4 Sep 2025

Optics EXPRESS

(MPLC) devices and carefully calibrating the optical paths, the inter-mode crosstalk was suppressed to <-25 dB. By employing Volterra pre-distortion, the intra-mode ISI were minimised, supporting a record-high 80 GBaud MDM transmission. By employing probabilistic shaping, the system achieved a record-high achievable information rate (AIR) of 4.49 Tbit/s/λ in all FSO communication systems.

The remainder of this paper is organised as follows. Section 2 described the experimental system. Section 3 detailed the optical setup and the method to calibrate the MDM FSO path. Section 4 described the DSP setup for our high-speed MDM transmissions. Section 5 provides the experimental results to demonstrate the 4.49 Tbit/s/λ MDM FSO system. Finally, Section 6 summarises the key advantages of the proposed system.

2. Experimental system

Our experimental MDM multiple-input multiple-output (MIMO) FSO communication system is depicted in Fig. 1. At the transmitter, a 1550.12 nm laser was modulated by a dual-polarisation (DP) in-phase and quadrature (IQ) modulator with a nominal 6 dB bandwidth of 45 GHz using a 4-channel 120 GSa/s arbitrary waveform generator (AWG) with a 3 dB bandwidth of 50 GHz, and a 80 GBaud signal was generated. The signal was root-raised cosine (RRC) shaped with a roll-off factor of 0.1 and pre-distorted by nonlinear Volterra pre-distortion [14,15]. The signal had a frame structure of 20,000 symbols with 1,920 quadrature phase-shift keying (QPSK) symbols in the training sequence, and 1 random QPSK pilot symbol for every 9 data symbols. The quadrature amplitude modulation (QAM) data symbols were either 16-QAM symbols generated from a $2^{15} - 1$ pseudo random binary sequence (PRBS) or probabilistic shaped 256-QAM symbols (shaping factor = 2, constellation entropy $\approx$ 7.32) generated from a mt19937ar Mersenne Twister [16]. After being amplified by an erbium-doped fiber amplifier (EDFA), the signals were passed through an acousto-optic modulator (AOM) to generate a 20 µs burst signal for each 160 µs period (Fig. 1(a1)) to enable the time-division multiplexing (TDM) receiver setup, which will be detailed later. To emulate independent transmitters, 6 copies were split from the burst signal and delayed by precisely calibrated variable fibre delay line (FDL). These delay lengths were carefully set to 0, 320, 640, 960, 1280, and 1600 symbols with an error of less than 0.05 symbol. Due to the FDL, only 320 of the 1,920 symbols in the training sequence were used for training purposes [12,17]. The delayed signals were passed through variable optical attenuator (VOA) to compensate for practical power imbalances at the inputs of MPLC. The compensated signals were then converted to corresponding HG modes using MPLC technology (Fig. 1(b)) [18]. The output beam waist diameter of the $HG_{0,0}$ mode was ~0.3 mm.

In the FSO channel shown in Fig. 1(a) and Fig. 1(c), the transmitted HG modes were passed through a beam expander consisting of a convex lens with a focal length of 30 mm (L1) followed by another convex lens with a focal length of 100 mm (L2). The expanded beam was reflected off a steering mirror (M1) with two high-precision stepper-motor actuators for precise alignment. The beam was then reflected off two more mirrors (M2, M3), and another symmetric beam expander consisting of a convex lens with a focal length of 100 mm (L3) followed by another convex lens with a focal length of 30 mm (L4). The beam was then coupled into the receiver MPLC device after a total FSO length of ~1.6 m.

At the receiver, the optical signals split by the receiver MPLC device were delayed by the FDL for the 6 lowest order modes to realise the TDM receiver. A 5 km difference between adjacent modes introduced a ~24.5 µs delay (Fig. 1(a2)), slightly longer than the signal burst (Fig. 1(a1)). Each delayed signal was then split by a 99:1 fibre coupler so that the overall power received by each mode could be measured by a corresponding power meter. The 6 lowest order modes were then amplified by 6 EDFA to compensate for the loss introduced by the receiver FDL and receiver coupler. The TDM signal was then amplified by another EDFA. Due to the attenuation introduced by the receiver FDL, it was inappropriate to reflect system performance

Optics EXPRESS

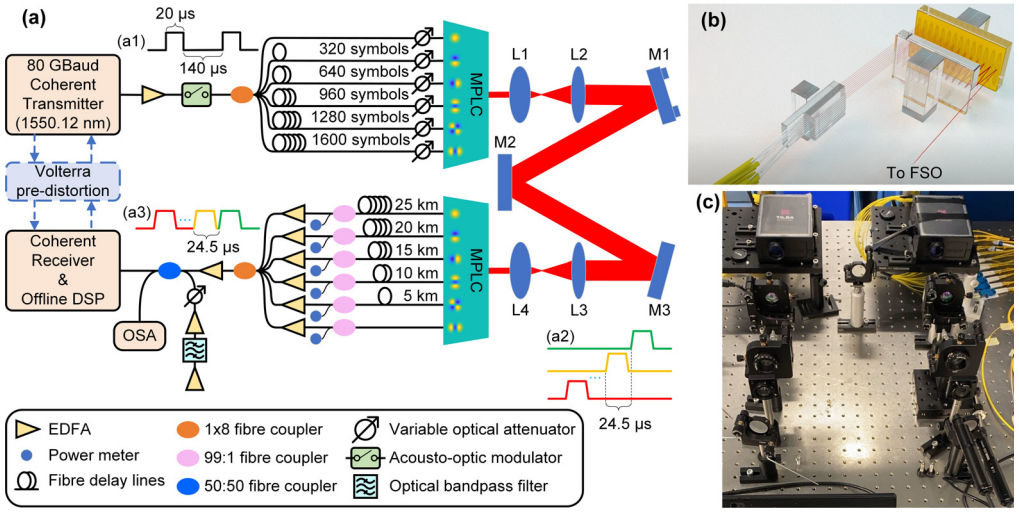

Fig. 1. Experimental setup for beaconless MDM communication system. L: lens; M: mirror; EDFA: erbium-doped fiber amplifier; MPLC: multi-plane light conversion; OSA: optical spectrum analyser; FSO: free-space optics. (a) Schematical diagram of experimental setup. (b) The structure of the MPLC device. (c) The normalised transfer matrix when the system is properly aligned.

by attenuating the transmitted signal. To examine the bit error rate (BER) performance versus optical signal-to-noise ratio (OSNR) when the system was optimally aligned, the variable optical noise was loaded by a sequence of devices involving an EDFA, an optical bandpass filter, another EDFA, a VOA, and a 50:50 coupler. The average OSNR was then assessed using an optical spectrum analyser (OSA) to facilitate OSNR scanning. Finally, the TDM signals were received by a coherent receiver with a 70 GHz, 200 GSa/s oscilloscope and demodulated by an offline DSP. The DSP includes a sequential combination of the Gram-Schmidt orthogonalisation [19], frequency-domain frequency offset estimation, frequency-domain chromatic dispersion (CD) compensation for the receiver FDL [20], Godard timing recovery [21], phase-asynchronous phase and channel estimation [22], and MIMO equalisation [23].

3. Optical path setup

Although MPLC demonstrated intrinsically low crosstalk and loss [18], the optical path requires stringent calibration to match the transmitted beam and the received beam. Our MPLC device has a beam waist radius of 150 μm for the $HG_{0,0}$ mode. Consider the Rayleigh length of the Gaussian beams:

$$z_R = \frac{\pi \omega_0^2 n}{\lambda}, \tag{1}$$

where ω_0 is the beam waist radius, n is the refraction index of the medium in which the beam propagates, and λ is the wavelength of the beam. The Rayleigh length of our MPLC device is approximately 0.046 m, too short to match the transmitted and received beam size. As shown in Fig. 2(a), beam expanders consisting of 2 convex lenses should be employed to increase the beam size along the FSO path. To optimally match the optical beam, the optical path should be symmetric (i.e. $d_1 = d_5$, $d_2 = d_4$, $f_1 = f_4$, and $f_2 = f_3$, where f_1, f_2, f_3, and f_4 are the focal lengths of the convex lenses L1, L2, L3, and L4, respectively). After being transmitted through path d_1, the beam is divergent at the input of lens L1. To match the beam size at the L2 and L3 lenses, the beam should be slightly convergent at the output of lens L2, so that the beam waist is located at

Optics EXPRESS

the centre of path d_3. Therefore, $d_2 > f_1 + f_2$ should be applied to match the convergence of the optimal path. By setting the total length of the FSO path $d = d_1 + d_2 + d_3 + d_4 + d_5 = 1.6\,\text{m}$, $d_1 = d_5 = 100\,\text{mm}$, $f_1 = f_4 = 30\,\text{mm}$, $f_2 = f_3 = 100\,\text{mm}$, which are consistent with our experimental setup, the optimal path length of d_2 was $d_{2,opt} \approx 140.74\,\text{mm}$ ($\sim$10.74 mm longer than $f_1 + f_2$). This optimal path length was obtained by employing the Gold-section search in the simulation [24], which employed Fourier optics to model the wave propagation and optimize the optical path length precisely [25].

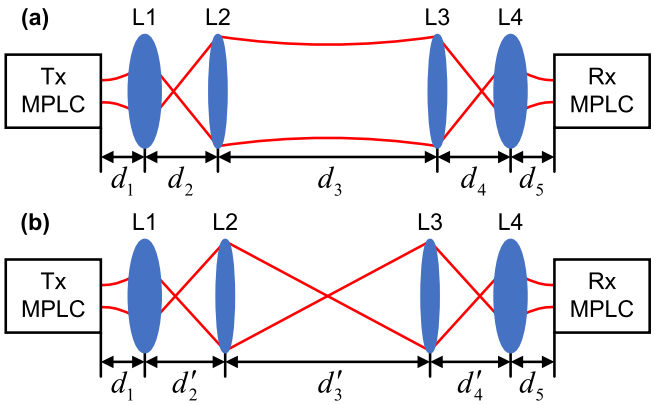

Fig. 2. The optical path with beam expanders. (a) The collimated case. (b) The converging case.

To investigate the sensitivity of the z-axis positioning of lenses L2 and L3, Fig. 3(a) depicted the relative power $P\left(HG_{0,0} \rightarrow HG_{0,0}\right)$ when d_2 and d_4 are slightly deviated from their optimal value by $d_2 = d_{2,opt} + \Delta d_2$ and $d_4 = d_{4,opt} + \Delta d_4$, respectively. As expected, there is a maximum relative power of 0 dB at $\Delta d_2 = \Delta d_4 = 0$. Moreover, there is another maximum at $\Delta d_2 = \Delta d_4 \approx 1.9\,\text{cm}$, which corresponds to the converging case shown in Fig. 2(b). In this case, the 2-dimensional beam profile will be rotated by 180° at the receiver. To better understand the importance of focal calibration, some important 1-dimensional cases are depicted in Fig. 3(b), including $\Delta d_4 = \Delta d_2$, $\Delta d_4 = -\Delta d_2$, $\Delta d_4 = 0$, and $\Delta d_4 = 1\,\text{cm}$. Corresponding to Fig. 3(a), we can observe 2 maximums when $\Delta d_4 = \Delta d_2$, indicating the collimated and converging cases, respectively. When $\Delta d_4 = -\Delta d_2$, or $\Delta d_4 = 0$, we observed one global maximum, indicating the larger deviation from the optimum point, the worse beam matching we will obtain. When comparing the two cases of $\Delta d_4 = 0$ and $\Delta d_4 = 1\,\text{cm}$, we can conclude that when the lens L3 deviates from the optimum location, the optimum location of the lens L2 will shift, indicating the necessity of recursively adjust both lenses to approach the global optimum.

When we employ $P\left(HG_{0,0} \rightarrow HG_{0,0}\right)$ to optimise the beam path, we notice a smooth area near the optimum point, making it difficult to minimise inter-mode crosstalk. Therefore, we need to investigate the performance of crosstalk to higher-order modes. The even-order modes (i.e. both mode orders are even numbers) are sensitive to the power leakage from $HG_{0,0}$ when the divergence is not optimally matched. While the odd-order modes (i.e. at least one of the mode orders is an odd number) are insensitive to divergence matching because of the different phase parity between these modes and $HG_{0,0}$. In Fig. 4(a), we plotted the relative power $P\left(HG_{0,0} \rightarrow HG_{2,0}\right)$ when d_2 and d_4 are slightly deviated from their optimal value by $d_2 = d_{2,opt} + \Delta d_2$ and $d_4 = d_{4,opt} + \Delta d_4$, respectively. some important 1-dimensional cases, including $\Delta d_4 = \Delta d_2$, $\Delta d_4 = -\Delta d_2$, and $\Delta d_4 = 0$, are also depicted in Fig. 4(b) for details. Opposite to the relative power performance of $HG_{0,0} \rightarrow HG_{0,0}$, here we observe two sharp minimums at the optimally collimated (Fig. 2(a))

Optics EXPRESS

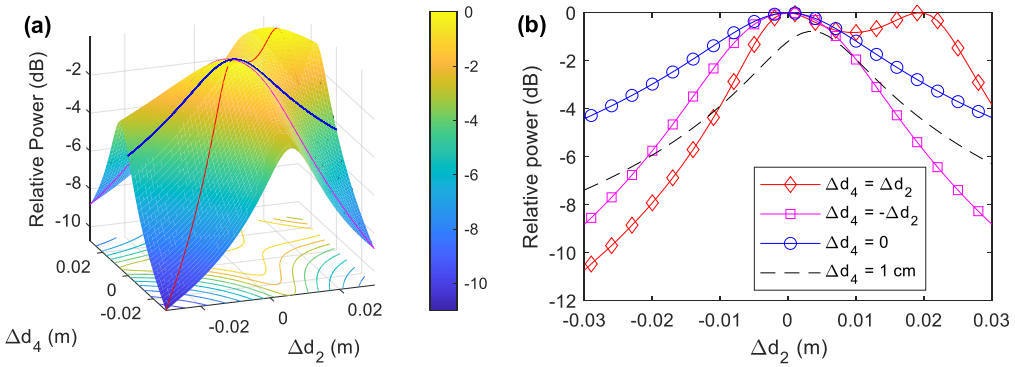

Fig. 3. Relative power $P\left(HG_{0,0} \rightarrow HG_{0,0}\right)$ versus Δd_2 and Δd_4. (a) 2-dimensional scanning; (b) 1-dimensional scanning

and converging (Fig. 2(b)) points, respectively. The sharp minimum at the optimally collimated point can be employed to fine-tune the optical path and minimise the inter-mode crosstalk.

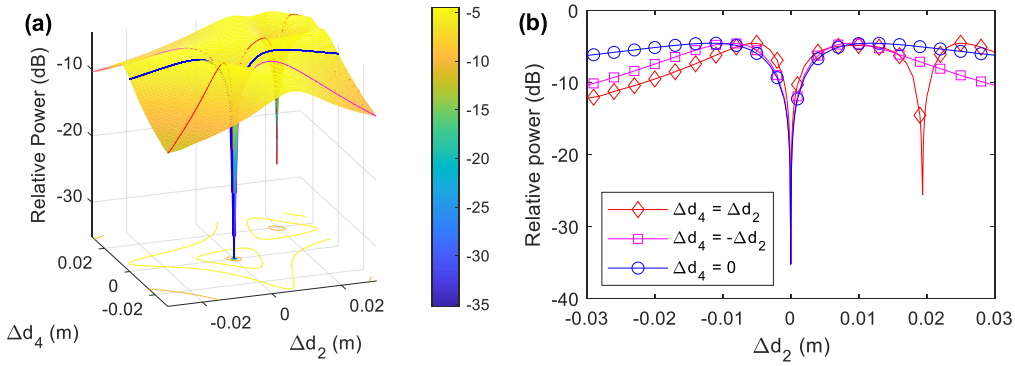

Fig. 4. Relative power $P\left(HG_{0,0} \rightarrow HG_{2,0}\right)$ versus Δd_2 and Δd_4. (a) 2-dimensional scanning; (b) 1-dimensional scanning

Moreover, as shown in Fig. 1(a), the tip-tilt calibration is also important to minimise the inter-mode crosstalk. This can be achieved by fine-tuning mirrors M1 and M3. Different from focal length matching, all higher-order modes are sensitive to tip-tilt mismatch, making it beneficial to observe the power leakage to all the higher-order modes in tip-tilt calibration. As a result, we should perform at least 6 primary degrees of freedom (DoF) for optical path calibration, including z-axis tuning for L2 and L3, and tip-tilt tuning for M1 and M3. It is also worth noting that all other mismatches, including tip-tilt and off-axis positioning of L1~L4, and z-axis positioning of L1 and L4, are secondary mismatches, which can be compensated by recursively adjusting the 6 primary DoF. As a result, the optical path can be calibrated by employing the process detailed in Algorithm 1. This algorithm relies on precise beam matching, which requires a turbulence-free environment over distances of less than a few hundred meters. Additionally, the practical link range must remain below twice the Rayleigh length, which is approximately 2.5 km when employing a Gaussian beam waist of 2.5 cm at the centre of the optical link.

Optics EXPRESS

Algorithm 1. The calibration process

Place devices according to calculation
Coarse calibration $\left(P\left(HG_{0,0} \rightarrow HG_{0,0}\right)\right)$:
repeat
  repeat
    Tune L2 for divergence
    Tune M1 and M3 for tip/tilt
  until $P\left(HG_{0,0} \rightarrow HG_{0,0}\right)$ is maximised
  repeat
    Tune L3 for divergence
    Tune M1 and M3 for tip/tilt
  until $P\left(HG_{0,0} \rightarrow HG_{0,0}\right)$ is maximised
until $P\left(HG_{0,0} \rightarrow HG_{2,0}\right)$ is sensitive
Fine calibration $\left(\sum_{(m,n)\neq(0,0)} P\left(HG_{0,0} \rightarrow HG_{m,n}\right)\right)$:
repeat
  repeat
    Tune L2 for divergence
    Tune M1 and M3 for tip/tilt
  until $\sum_{(m,n)\neq(0,0)} P\left(HG_{0,0} \rightarrow HG_{m,n}\right)$ is minimised
  repeat
    Tune L3 for divergence
    Tune M1 and M3 for tip/tilt
  until $\sum_{(m,n)\neq(0,0)} P\left(HG_{0,0} \rightarrow HG_{m,n}\right)$ is minimised
until $\sum_{(m,n)\neq(0,0)} P\left(HG_{0,0} \rightarrow HG_{m,n}\right)$ is satisfied

4. Digital signal processing algorithms

4.1. Volterra pre-distortion

To compensate for the nonlinear effects in the components of our optical transceiver, the transmitted signal was pre-distorted by nonlinear Volterra pre-distortion with kernel memory lengths of (201,9,9) taps. As a result, $201 + 9^2 + 9^3 = 1011$ coefficients will be generated and $201 + 2 \times 9^2 + 3 \times 9^3 = 2550$ multiplications will be consumed for the pre-distortion. As shown in Fig. 5, we employed an indirect learning architecture (ILA) for Volterra coefficients training [14]. Here we pre-distorted the signal $s(n)$ by

$$\begin{aligned} p(n) = &\sum_{j=-N_1}^{N_1} v_j s(n-j) + \sum_{j=-N_2}^{N_2} \sum_{k=j}^{N_2} v_{j,k} s(n-j)\, s(n-k) \\ &+ \cdots + \sum_{j=-N_3}^{N_3} \sum_{k=j}^{N_3} \sum_{l=k}^{N_3} v_{j,k,l} s(n-j)\, s(n-k)\, s(n-l), \end{aligned} \tag{2}$$

where v_j, $v_{j,k}$, and $v_{j,k,l}$ are the 1^{st}, 2^{nd}, and 3^{rd} order coefficients of the Volterra pre-distorter, respectively, $(2N_1 + 1, 2N_2 + 1, 2N_3 + 1) = (201, 9, 9)$ is the tap length of the Volterra pre-distorter. After training the Volterra pre-distorter, we should obtain $y(n) \rightarrow s(n)$, and thus $e(n) = p(n) - o(n) \rightarrow 0$. To achieve these goals, there are 2 iterations in the training stage:

1. Iterate on the Volterra model $\mathbf{V}$ according to $e(n)$;
2. Update the copy of $\mathbf{V}$ and repeat step 1.

Optics EXPRESS

In our system, the nominal 6 dB bandwidth of the DP-IQ modulator was 45 GHz, reasonably lower than half of the AWG sample rate 120 GSa/s. Therefore, if we employ a probe signal of 120 GBaud, the significant attenuation of the high-frequency components will introduce imbalanced power output between in-phase and quadrature components, as well as x- and y-polarisations. On the other hand, if we employ a probe signal of 80 GBaud, which is the same as our transmitted signal, the performance at the transition area near 40 GHz will be sub-optimally pre-distorted. To obtain the optimal BER performance in our back-to-back system, we employed the first 2 updates in step 2 (update the copy of **V**) by employing the 120 GBaud probe signals for coarse training, and the rest of the updates in step 2 (update the copy of **V**) by employing the 80 GBaud probe for fine training. In both steps, 10^6 samples were recorded to guarantee the convergence of the pre-distorter. The probe signal was 16-QAM signals generated from $2^{15} - 1$ PRBS for nonlinear system identification. Compared with the S-parameter compensation, approximately 3 dB effective signal-to-noise ratio (SNR) improvement was observed in our system in the high OSNR area when employing the Volterra pre-distortion algorithm.

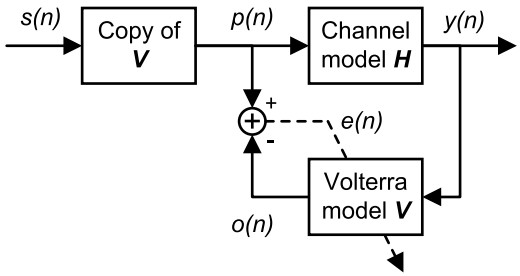

Fig. 5. The indirect learning architecture of the Volterra pre-distorter.

4.2. Probabilistic shaping

The probabilistic shaping (PS) can be applied to constellation diagrams to maximise the AIR of an optical communication system [26]. An optimised probability mass function (PMF) for probabilistic shaping is

$$P_X(x_i) = \frac{1}{\sum_{x_j \in \mathcal{X}} e^{-\nu |x_j|^2}} e^{-\nu |x_i|^2}, \tag{3}$$

where x_i is the i^{th} constellation point of a normalised QAM signal set $\mathcal{X}$, and ν is the shaping factor. In an experimental system, a fixed shaping factor is preferable because the transmitter can be fixed for a fair comparison at different OSNR. If we set $\nu = 2$, the generalized mutual information (GMI) of an additive white Gaussian noise (AWGN) channel can be depicted in Fig. 6. When compared with the AWGN capacity, a 0.1 dB penalty is observed at 2.26 bit/symbol for PS-16-QAM, 4.09 bit/symbol for PS-64-QAM, and 6.34 bit/symbol for PS-256-QAM, respectively. In our experimental system, the GMI can achieve more than 5.3 bit/symbol. Therefore, we chose PS-256-QAM when probabilistic shaping was employed in our experiments.

Optics EXPRESS

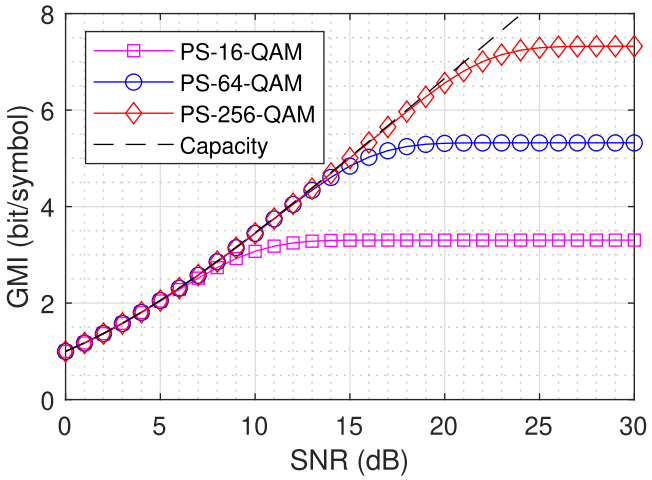

Fig. 6. The generalized mutual information (GMI) of different modulation formats.

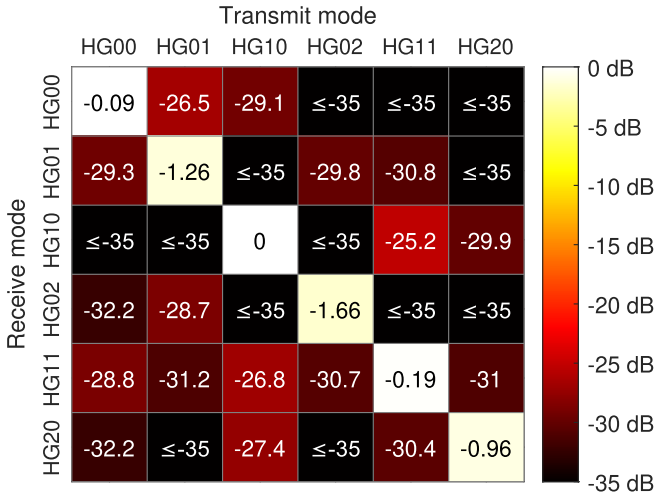

Fig. 7. The normalised transfer matrix when the FSO system is optimally aligned.

5. Experimental results

By employing Algorithm 1 and corresponding principles detailed in Section 3, we can optimise the FSO path. Figure 7 depicts the normalised transfer matrix when the FSO path is optimally calibrated. Here, we achieved <1.7 dB mode-dependent loss, and >25 dB suppression for 6×6 MIMO, indicating a good inter-mode crosstalk suppression in our experimental system. Although we only focused on the transfer matrix taken from the receiver, the reciprocity of light automatically guarantees an optimal transfer matrix taken from the transmitter when the system is optimally aligned.

The experimental results of the communication performance are depicted in Fig. 8. Considering 16-QAM signals without noise loading, the channel-wise constellation diagrams are shown in Fig. 8(a). When the FSO system was optimally aligned, the error vector magnitude (EVM)

Optics EXPRESS

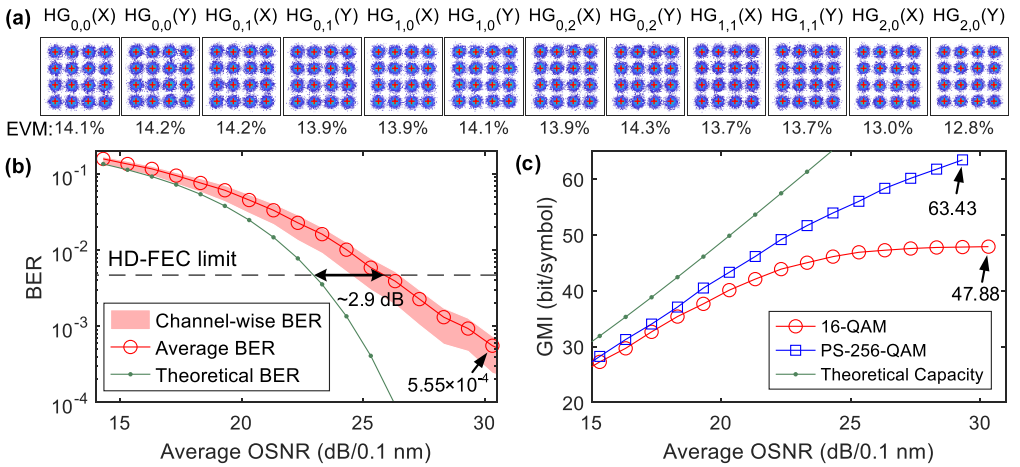

Fig. 8. Experimental results of the communication system. EVM: error vector magnitude; BER: bit error rate; OSNR: optical signal-to-noise ratio; HD-FEC: hard-decision forward error correction; GMI: generalized mutual information. (a) Constellation diagram. Red crosses: reference constellation points. (b) BER versus average OSNR for 16-QAM. (c) GMI versus average OSNR.

performance across different channels was similar, with minor differences observed due to the mode-dependent loss in the MPLC devices.

Figure 8(b) depicts the average BER versus the average OSNR when loading 16-QAM signals. We observe an implementation penalty of <3 dB at the hard-decision forward error correction (HD-FEC) limit of 4.7×10^{-3} [27]. We believe this was mainly due to (1) the shot noise and quantisation noise in the coherent receiver; (2) the DSP implementation penalty; (3) the mode-dependent loss in the MPLC devices. To quantify the influence of mode-dependent loss, we illustrate the range of channel-wise BER with a shaded pink area in Fig. 8(b). We observed slight BER fluctuations between different channels, which was consistent with the EVM fluctuations in Fig. 8(a). In the high OSNR area, a minimum average BER of 5.55×10^{-4} was obtained, approximately an order of magnitude lower than the HD-FEC limit.

Figure 8(c) depicts the aggregate GMI versus the average OSNR when loading 16-QAM signals and PS-256-QAM signals, respectively. In the low OSNR area, the experimental GMI aligned with the theoretical capacity, with approximately 1.13 dB and 1.56 dB OSNR degradation for PS-256-QAM signals and 16-QAM signals, respectively. We believe the 1.13 dB degradation mainly came from the practical implementation penalty and the further 0.43 dB degradation for 16-QAM signals mainly came from the constellation penalty. In the high OSNR area, the 16-QAM signals achieved a GMI of 47.88 bit/symbol, approaching the theoretical limit of 6 modes × 2 polarisations × 4 bit/symbol = 48 bit/symbol. When loading the PS-256-QAM signals, the GMI was further increased to 63.43 bit/symbol in the high OSNR area, while a higher deviation was observed from the theoretical capacity due to the practical implementation penalties. Taking into account the 1.6% operationally employed training sequence (320 out of 1,920 symbols) and the 10% pilot rate, an AIR of 3.39 Tbit/s/λ for 16-QAM systems and 4.49 Tbit/s/λ for PS-256-QAM systems was achieved when transmitting 80 GBaud signals.

6. Conclusion

In this paper, we have proposed a novel optical calibration algorithm for a high symbol rate 6 × 6 HG-MDM FSO communication system. By employing MPLC-based mode-(de)multiplexer

Optics EXPRESS

and carefully calibrating the optical path, the inter-mode crosstalk was suppressed to <-25 dB. Moreover, the intra-mode ISI were minimised by employing Volterra pre-distortion. As a result, our system supported up to 80 GBaud signals, achieving a record-high AIR of 4.49 Tbit/s/λ when loading PS-256-QAM signals, and 3.39 Tbit/s/λ when loading 16-QAM signals, respectively. These results indicated the feasibility of employing MDM technology for ultra-high capacity wireless communications in relatively short distances, which is suitable for intra-data centre applications and short inter-building links. Considering the potential turbulence resiliency in MDM systems, the ultra-high-speed MDM transmission could also be extended to long-distance applications in the future. Noting the successful demonstration of combining polarisation, wavelength and spatial multiplexing in few-mode fibre links [6], it is also possible to combine all these multiplexing technologies for Peta-bit-per-second FSO links in future applications.

Funding. Engineering and Physical Sciences Research Council (EP/T009047/1, EP/S003436/1, EP/S016171/1); European Regional Development Fund (CENTRO-01-0145-FEDER-022141); Fundação para a Ciência e a Tecnologia (PTDC/EEI-TEL/2697/2021, 2022.07168.CEECIND); H2020 Marie Skłodowska-Curie Actions (10100828, 713694).

Acknowledgments. We thank Dr. Zhaozhong Chen and Dr. Chao Gao for fruitful discussions.

Disclosures. The authors declare no conflicts of interest.

Data availability. Data underlying the results presented in this paper are not publicly available at this time but may be obtained from the authors upon reasonable request.

References

1. J. Wang, J.-Y. Yang, I. M. Fazal, *et al.*, "Terabit free-space data transmission employing orbital angular momentum multiplexing," Nat. Photonics **6**(7), 488–496 (2012).
2. W. Ali, G. Cossu, L. Gilli, *et al.*, "10 Gbit/s OWC system for intra-data centers links," IEEE Photonics Technol. Lett. **31**(11), 805–808 (2019).
3. R. Lange, B. Smutny, B. Wandernoth, *et al.*, "142 km, 5.625 Gbps free-space optical link based on homodyne BPSK modulation," in *Free-space laser communication technologies XVIII*, vol. 6105 (SPIE, 2006), pp.68–76.
4. B. I. Bitachon, Y. Horst, L. Kulmer, *et al.*, "Tbit/s single channel 53 km free-space optical transmission-assessing the feasibility of optical GEO-satellite feeder links," in *European Conference and Exhibition on Optical Communication*, (Optica Publishing Group, 2022), pp.Th3A–6.
5. E. Ciaramella, Y. Arimoto, G. Contestabile, *et al.*, "1.28 Terabit/s (32x40 Gbit/s) WDM transmission system for free space optical communications," IEEE Journal on selected areas in communications **27**(9), 1639–1645 (2009).
6. G. Rademacher, B. J. Puttnam, R. S. Luís, *et al.*, "Peta-bit-per-second optical communications system using a standard cladding diameter 15-mode fiber," Nat. Commun. **12**(1), 4238 (2021).
7. K. Pang, H. Song, Z. Zhao, *et al.*, "400-Gbit/s QPSK free-space optical communication link based on four-fold multiplexing of Hermite–Gaussian or Laguerre–Gaussian modes by varying both modal indices," Opt. Lett. **43**(16), 3889–3892 (2018).
8. Y. Li, Z. Chen, D. M. Benton, *et al.*, "Single-wavelength polarization-and mode-division multiplexing free-space optical communication at 689 Gbit/s in strong turbulent channels," Opt. Lett. **48**(13), 3575–3578 (2023).
9. N. Zhao, X. Li, G. Li, *et al.*, "Capacity limits of spatially multiplexed free-space communication," Nat. Photonics **9**(12), 822–826 (2015).
10. M. A. Fernandes, P. P. Monteiro, and F. P. Guiomar, "Free-space terabit optical interconnects," J. Lightwave Technol. **40**(5), 1519–1526 (2022).
11. M. M. Abadi, M. A. Cox, R. E. Alsaigh, *et al.*, "A space division multiplexed free-space-optical communication system that can auto-locate and fully self align with a remote transceiver," Sci. Rep. **9**(1), 19687 (2019).
12. Z. Hu, Y. Li, D. M. Benton, *et al.*, "Single-wavelength transmission at 1.1-Tbit/s net data rate over a multi-modal free-space optical link using commercial devices," Opt. Lett. **47**(14), 3495–3498 (2022).
13. Y. Ren, Z. Wang, P. Liao, *et al.*, "Experimental characterization of a 400 Gbit/s orbital angular momentum multiplexed free-space optical link over 120 m," Opt. Lett. **41**(3), 622–625 (2016).
14. C. Eun and E. J. Powers, "A new Volterra predistorter based on the indirect learning architecture," IEEE transactions on signal processing **45**(1), 223–227 (1997).
15. M. Nölle, M. S. Erkılınç, R. Emmerich, *et al.*, "Characterization and linearization of high bandwidth integrated optical transmitter modules," in *2020 European Conference on Optical Communications (ECOC)*, (IEEE, 2020), pp.1–4.
16. M. Matsumoto and T. Nishimura, "Mersenne twister: a 623-dimensionally equidistributed uniform pseudo-random number generator," ACM Transactions on Modeling and Computer Simulation (TOMACS) **8**(1), 3–30 (1998).
17. Y. Li, Z. Chen, Z. Hu, *et al.*, "Enhanced atmospheric turbulence resiliency with successive interference cancellation DSP in mode division multiplexing free-space optical links," J. Lightwave Technol. **40**(24), 7769–7778 (2022).
18. N. K. Fontaine, R. Ryf, H. Chen, *et al.*, "Laguerre-Gaussian mode sorter," Nat. Commun. **10**(1), 1865 (2019).

Optics EXPRESS

19. I. Fatadin, S. J. Savory, and D. Ives, "Compensation of quadrature imbalance in an optical QPSK coherent receiver," IEEE Photonics Technol. Lett. **20**(20), 1733–1735 (2008).
20. M. S. Faruk and S. J. Savory, "Digital signal processing for coherent transceivers employing multilevel formats," J. Lightwave Technol. **35**(5), 1125–1141 (2017).
21. D. Godard, "Passband timing recovery in an all-digital modem receiver," IEEE Transactions on Communications **26**(5), 517–523 (1978).
22. Y. Li, Z. Chen, M. Patel, *et al.*, "Phase and channel estimation for high-capacity phase-asynchronous mode-division multiplexing multiple-input multiple-output free-space optical communications in strong turbulent channels," J. Lightwave Technol. **42**(11), 4132–4143 (2024).
23. S. Randel, R. Ryf, A. Sierra, *et al.*, "6× 56-Gb/s mode-division multiplexed transmission over 33-km few-mode fiber enabled by 6× 6 MIMO equalization," Opt. Express **19**(17), 16697–16707 (2011).
24. J. Kiefer, "Sequential minimax search for a maximum," Proc. Am. Math. Soc. **4**(3), 502–506 (1953).
25. J. W. Goodman, *Introduction to Fourier optics* (Roberts and Company publishers, 2005).
26. T. Fehenberger, A. Alvarado, G. Böcherer, *et al.*, "On probabilistic shaping of quadrature amplitude modulation for the nonlinear fiber channel," J. Lightwave Technol. **34**(21), 5063–5073 (2016).
27. A. Alvarado, E. Agrell, D. Lavery, *et al.*, "Replacing the soft-decision FEC limit paradigm in the design of optical communication systems," J. Lightwave Technol. **33**(20), 4338–4352 (2015).